chemistry

MDPI

Article

Modification of the Bridging Unit in Luminescent Pt(II) Complexes Bearing C^N*N and C^N*N^C Ligands

Stefan Buss [1,2], María Victoria Cappellari [1,2], Alexander Hepp [1], Jutta Kösters [1] and Cristian A. Strassert [1,2,*]

[1] Institut für Anorganische und Analytische Chemie, Westfälische Wilhelms-Universität Münster, Corrensstraße 28/30, 48149 Münster, Germany
[2] CeNTech, CiMIC, SoN, Westfälische Wilhelms-Universität Münster, Heisenbergstraße 11, 48149 Münster, Germany
* Correspondence: ca.s@wwu.de

Abstract: In this work, we explored the synthesis and characterization of Pt(II) complexes bearing different tri- and tetradentate luminophores acting as C^N*N- and C^N*N^C-chelators. Thus, we investigated diverse substitution patterns in order to improve their processability and assessed the effects of structural variations on their excited state properties. Hence, a detailed analysis of the different synthetic pathways is presented; the photophysical properties were studied by using steady-state and time-resolved photoluminescence spectroscopy. We determined the absorption and emission spectra, the photoluminescence efficiencies, and the excited state lifetimes of the complexes in fluid solutions at room temperature and frozen glassy matrices at 77 K. Finally, a structure–property relationship was established, showing that the decoration of the bridging unit on the tridentate luminophores only marginally affects the excited state properties, whereas the double cyclometallation related to the tetradentate chelator prolongs the excited state lifetime and increases the photoluminescence quantum yield.

Keywords: soluble triplet emitters; synthesis of Pt(II) complexes; (time-resolved) photoluminescence spectroscopy

check for updates

Citation: Buss, S.; Cappellari, M.V.; Hepp, A.; Kösters, J.; Strassert, C.A. Modification of the Bridging Unit in Luminescent Pt(II) Complexes Bearing C^N*N and C^N*N^C Ligands. *Chemistry* **2023**, *5*, 1243–1255. https://doi.org/10.3390/chemistry5020084

Academic Editor: Catherine Housecroft

Received: 1 April 2023
Revised: 8 May 2023
Accepted: 8 May 2023
Published: 15 May 2023

Copyright: © 2023 by the authors. Licensee MDPI, Basel, Switzerland. This article is an open access article distributed under the terms and conditions of the Creative Commons Attribution (CC BY) license (https://creativecommons.org/licenses/by/4.0/).

1. Introduction

In recent years, triplet emitters have received increasing attention due to their range of different applications relying on their balance between solubility and tendency towards aggregation [1–6]. Among organometallic compounds, Pt(II) complexes represent a special case where the intrinsic high ligand field splitting (LFS) and strong spin-orbit coupling (SOC) on the metal center lead to desirable photophysical properties, such as long excited state lifetimes and high photoluminescence quantum yields [7–13]. In addition, the d^8 configuration of the Pt(II) center leads to square planar coordination geometries, leaving the $d_z{}^2$ orbitals available for intermolecular coupling of the metal atoms. Hence, the aggregation properties of these complexes can be exploited in the context of supramolecular approaches by harnessing the unique characteristics of triplet states delocalized over dimeric species [14–16]. These concepts have been used for OLED fabrication [17–22], photocatalysis [7,23–26], bioimaging [27–29], and sensing technologies [30–33], among others.

As mentioned above, a high LFS plays an important role, as it increases the energy of dissociative metal-centered (MC) excited states to prevent thermally activated deactivation processes involving radiationless pathways that shorten the excited state lifetimes while reducing the efficiency of more desirable mechanisms [34]. In this regard, phenide-based σ-donors (cyclometalated aryl-functions) are widely used to increase the LFS due to their negative charge [35]. In addition, the rigidity of the chromophoric ligand contributes to the overall performance; hence, complexes bearing tri- and tetradentate chelators are preferred [34]. While tetradentate ligands lead to highly stable complexes and show an

overall better performance, complexes with tridentate ligands can show tunable properties depending on the monodentate co-ligand, which can be adjusted depending on the intended outcome [14–16,36].

Huo et al. reported on studies focused on the optimization of the coordination environment derived from tri- and tetradentate ligands for Pt(II). Hence, they synthesized complexes with a combination of five- and six-membered metalacycles (including bis-cyclometalation for the tetradentate ligands) displaying interesting photophysical properties (Figure 1) [37,38]. Inspired by the work of Huo et al., we explored different alternative concepts. For instance, we decorated the cyclometalating unit with fluorine atoms to adjust the emission wavelength as well as the aggregation behavior (Figure 1) [39].

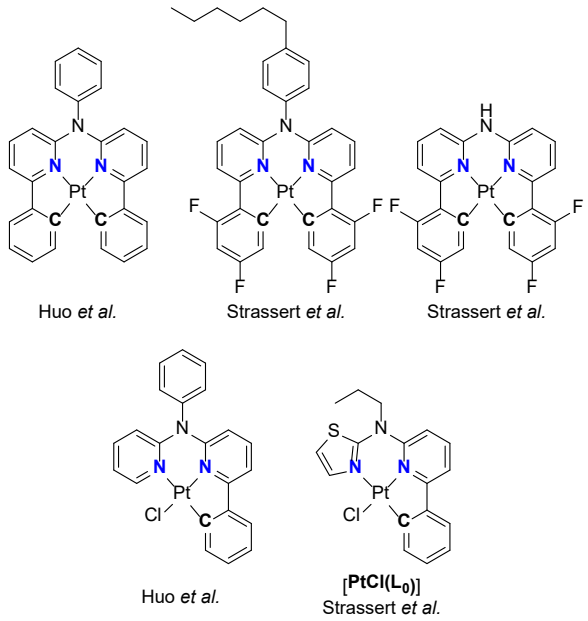

Figure 1. Selected Pt(II) complexes from previous studies. **Top**: CˆN*NˆC-based complexes with phenyl-amine (left) [37], 4-hexylphenyl-amine (center) [39], and secondary amine (right) [40] bridges. **Bottom**: N*NˆC complexes with phenyl-amine (left) and [38] propyl-amine connectors (right; **[PtCl(L$_0$)]**) [41].

In 2019, we reported the synthesis of a bis-cyclometalated Pt(II) complex bearing a tetradentate ligand with a secondary amine bridge (Figure 1) [40]. Additionally, in 2020, the synthesis of Pt(II) complexes with CˆN*N luminophores based on thiazol moieties was reported (Figure 1) [41]. In the present work, we aimed at an improvement of their rather low solubility while maintaining the planar coordination environment, and we designed a synthetic route to introduce a secondary amine that is subsequently functionalized by an alkylation step. Since the range of commercially available alkyl-bromides is wide, the alkylation reaction could provide a versatile tool to enable a vast range of decoration patterns. In this report, the impact on the chemical and photophysical properties of the resulting complexes was also investigated.

2. Experimental Section

General information about experimental procedures including instrumental and synthetic methods, structural characterization of the ligand precursors and the complexes, as well as photophysical measurements are provided in the Supplementary Materials.

Materials: All chemicals were used as purchased from commercially available sources. For the photophysical measurements, spectroscopic-grade solvents (Uvasol®) were used.

Synthesis: The detailed synthetic procedures and analytical data are provided in the Supplementary Materials. Each new compound was characterized by ^{1}H, ^{13}C, and

2D nuclear magnetic resonance spectroscopies (NMR, see Figures S1–S106) as well as mass spectrometry (EM-ESI-MS or MALDI-MS). The metal complexes were further analyzed by steady-state and time-resolved photoluminescence spectroscopy.

X-ray diffractometry: Suitable single crystals for X-ray diffraction measurements were obtained by slowly evaporating the solvent from a saturated DCM solution or by the diffusion of cyclohexane into such a solution; in the case of **[PtCl(L$_4$)]**, the complex was crystallized from diethylether. The full set of data is given in the Supplementary Materials (Tables S1–S4; Figures S107–S114), as well as in the CCDC database (CCDC-Nr. 2252944 (**I$_1$**), 2252945 (**A$_4$**), 2252950 (**A$_3$**), 2252953 (**[PtL$_6$]**), 2252954 (**[PtCl(L$_4$)]**), 2252967 (**[PtCl(L$_2$)]**). The graphical representation of the molecular structures was realized by using the Mercury software package from CCDC [42].

3. Results and Discussion

With the selected precursors (**A$_5$**, **A$_6$**), we were able to establish a three-step synthesis route, based on our previous report [41], yielding complexes bearing tri- and tetradentate ligands.

3.1. Tridentate Coordination

The first step in the synthesis of the tridentate ligands involves the alkylation of the secondary amine **A$_5$** by a previously described procedure [41]. Due to the tautomeric equilibrium involving the 2-amino thiazole unit, this reaction produces both an amine (**A$_x$**) and an imine (**I$_x$**) [41,43,44]. The observed ratios of A/I yields suggest that the formation of imines is favored when bulkier alkylbromides are employed. The molecular structures in the single crystals of **I$_1$** and **A$_3$** are depicted in Figure 2; both show a coplanar orientation of the heterocycles (for further information, see Figures S107–S108 and Table S1 in the Supplementary Materials). The two isomers can be easily distinguished by the $^3J_{HH}$-coupling constant in the ^{1}H-NMR spectrum, as the amine has a value of $^3J_{HH}$ = 3.6 Hz, whereas the imine reaches $^3J_{HH}$ = 4.8 Hz. Interestingly, the coordination of the thiazole on the metal center leads to a constant of around $^3J_{HH}$ = 4.1 Hz (*vide infra*). The formation of the two species was one of the main drawbacks of these reactions, due to the loss of significant amounts of potential products. Therefore, we explored the post-functionalization of the secondary amino group by acylation. By dissolving **A$_5$** in hot valeric anhydride, the formation of the amide **A$_4$** was achieved without the formation of the imine-like tautomer; the moderate yields are due to the incomplete conversion of the precursor. The amide **A$_4$** is a crystalline white solid, its molecular structure in the single crystal is shown in Figure 2 (see also Figure S109 in the Supplementary Materials, as well as Table S1), and it is clear that the thiazolyl moiety is coplanar with the amide, whereas the pyridine is bent out of plane. Subsequent attempts to reduce the amide to yield an amine failed with various reagents (LiAH, $NaBH_4$, BH_3·THF, $SiEt_3H$), as only the secondary amine **A$_5$** was obtained. Nonetheless, with the four amine precursors in hand, the versatile Suzuki–Miyaura coupling reactions with suitable boronic acids led to the four tridentate ligand precursors (**L$_x$H**). For the alkyl-substituted precursors (**L$_1$H**-**L$_3$H**), the final cyclometallation step was carried out using well-established reaction conditions (i.e., glacial acetic acid as a solvent at reflux paired with $K_2[PtCl_4]$), which successfully yielded the complexes **[PtCl(L$_X$)]**. The low yield of **[PtCl(L$_1$)]** can be attributed to the worse solubility and higher retention time during column chromatographic purification. In the case of **[PtCl(L$_3$)]**, the low yield seems to originate from the acid-mediated lability of the benzylic group [45]. On the other hand, the acylated ligand precursor **L$_4$H** was unstable under the cyclometallation conditions and only the complex **[PtCl(L$_5$)]** was formed, as the amide was cleaved towards the complex with a secondary amine. In order to obtain the desired amide-substituted complex **[PtCl(L$_4$)]**, milder conditions were used (i.e., MeCN/H_2O at reflux). The synthesis scheme is summarized in Figure 2 [46]. Regarding the solubility of these compounds, compared to the already published propyl-substituted complex [41], the methyl-substituted species (**[PtCl(L$_1$)]**) and the free secondary amine (**[PtCl(L$_5$)]**) presented poorer solubility; quite surprisingly, the 3,3-dimethyl-butyl complex (**[PtCl(L$_2$)]**) is comparable

to the already-reported compound. The last two complexes ([**PtCl(L$_3$)**], [**PtCl(L$_4$)**]) showed better solubility than the other exemplars; unfortunately, they correspond to the least stable ligands under the explored reaction conditions.

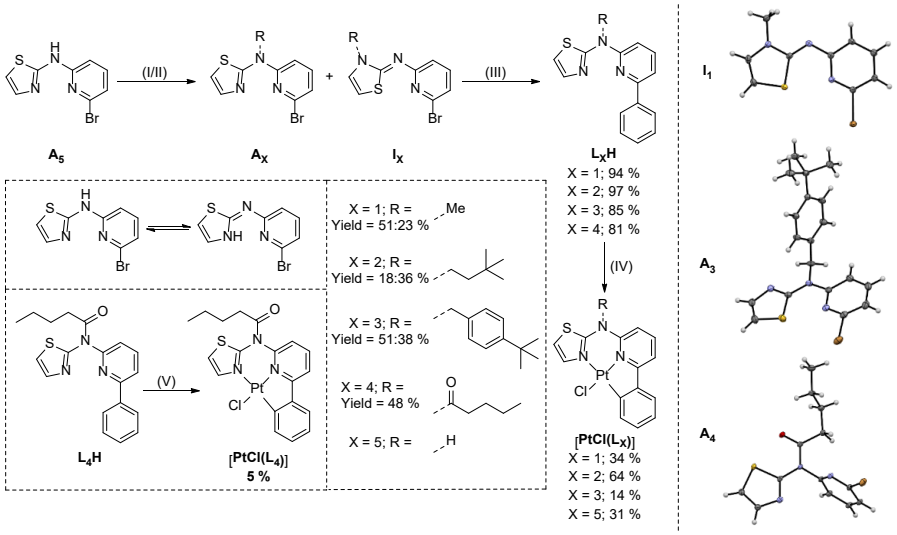

Figure 2. **Left**—Reaction schemes for the synthesis of the complexes with tridentate ligands. (I) Alkylation: bromoalkane, Cs_2CO_3, THF, reflux, 16 h, 18–51% yield. (II) Acylation: valeric anhydride, 170 °C, 3 h, 48%. (III) Suzuki–Miyaura cross-coupling: phenyl-boronic acid, K_2CO_3, [$Pd(PPh_3)_4$], THF, H_2O, reflux, 16 h, 81–97% yield. (IV) Cyclometallation: $K_2[PtCl_4]$, $^nBu_4NCl$, glacial acetic acid, reflux, 16 h, 14–64% yield. (V) Cyclometallation: $K_2[PtCl_4]$, MeCN/H_2O, reflux, 16 h, 5% yield. **Right**—Molecular structure in single crystals of **I$_1$** (top), **A$_3$** (center), and **A$_4$** (bottom). Displacement ellipsoids are shown at 50% probability.

We were able to obtain the molecular structures of [**PtCl(L$_2$)**] and [**PtCl(L$_4$)**] in single crystals by X-ray diffractometry, as shown in Figures 3 and 4, respectively (further details are found in the Supplementary Materials, Figures S110–S113 and Tables S2 and S3). The crystal structure of [**PtCl(L$_2$)**] corresponds to the $P2_1/c$ space group and confirms the square planar coordination environment with a chlorido unit as the fourth ligand. The overall coordination geometry is practically square planar, in agreement with the previously reported propyl-substituted complex [**PtCl(L$_0$)**]. Also in the present study, the formation of head-to-tail dimers is apparent. However, in this case, the 3D packing arises from the interactions between the π system and the hydrogen atoms, rather than being a chain evolving from stacked dimers in one direction supported by H-π interactions [41].

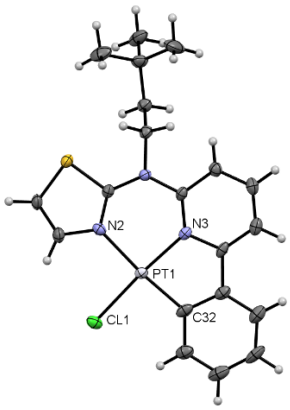

Figure 3. Molecular structure in the single crystal of [**PtCl(L$_2$)**]. Displacement ellipsoids are shown at 50% probability.

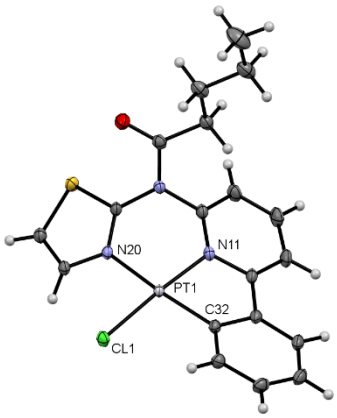

Figure 4. Molecular structure in the single crystal of **[PtCl(L$_4$)]**. Displacement ellipsoids are shown at 50% probability.

The crystal structure of the complex **[PtCl(L$_4$)]** involves three distinguishable conformers of the monomeric units, which crystallize in the $P\bar{1}$ space group. The coordination of the Pt(II) center in the case of **[PtCl(L$_4$)]** (i.e., one tridentate chromophore and one chlorido co-ligand) shows that the forced planarity of the amide bridge leads to an increased sterical demand for the chain and results in the bending of the chelating ligand. To release the sterical strain, the phenylpyridine and the thiazole moiety bend out of the coordination plane, which is visible in the higher deviation of the bond angle (N20-Pt1-C32 = 168.36°; for **[PtCl(L$_2$)] =** 175.97°) from the optimal 180° coordination geometry. The main differences between the three conformers are the placement and orientation of the alkyl group. The main intermolecular interactions for the 3D structure are the π–π interactions from the phenylpyrindine luminophores, combined with van der Waals interactions. Overall, no significant Pt-Pt coupling can be traced. The higher sterical strain, if compared with the alkyl-substituted analogs, in combination with the intrinsic reactivity of the amide in the presence of acids, may lead to the lability of the ligand during the cyclometalating reaction.

3.2. Tetradentate Coordination

The remarkable photophysical properties of Pt(II) complexes with CˆN*NˆC-type ligands are attributed to the large LFS and rigidity of the coordination environment [38]. For these luminophoric chelators, the Buchwald–Hartwig reaction limits the substitution pattern to aryl-amines and restricts the potential of substituents to enhance the processability of the complexes. In this sense, hexyl-phenyl substituents were necessary to attain meaningful solubility in organic solvents [39,40].

We therefore developed a synthetic approach similar to the one used for the herein-described tridentate thiazole-based compounds, but with a proper adaptation for tetradentate bis-cyclometalating ligand precursors. In this way, the Buchwald–Hartwig cross-coupling is avoided while giving access to alkyl-substitution on the bridging nitrogen atom. The di(bromo-pyridine)amine precursor is known from the literature [40,47] and can be modified as in the case of **A$_5$**. The alkylation can be achieved by following the procedure reported in the literature, using an alkylbromide and NaH in DMF at room temperature, thus yielding **A$_6$** [47]. The second step again involves a Suzuki–Miyaura cross-coupling towards the tetradentate ligand precursor **L$_6$H$_2$**. Unfortunately, the incomplete conversion leads to a product mixture of the di-substituted **L$_6$H$_2$** and the mono-substituted **L$_6$BrH** species. This explains the relatively low yields; nonetheless, the remaining bromine atom could represent a versatile intermediate where a second functionalization step could provide an asymmetric tetradentate chelator with interesting photophysical properties [48]. In the final step, the cyclometalation yielded the complex **[Pt(L$_6$)]**; due to the double cyclometalation, the reaction time needs to be adjusted to ensure a reasonable yield (from 16 h to 48 h; the synthesis is summarized in Figure 5). From pure DCM, we were able to obtain suitable

crystals for X-ray diffractometry (the molecular structure in the crystal is shown in Figure 6; more details can be found in the Supplementary Materials, see Figure S114 and Table S4). The crystal structure shows a packing resembling **[PtCl(L$_2$)]**, as both crystalize in a $P2_1/c$ space group, forming head-to-tail-dimers where the 3D packing results from interactions between the π systems and the hydrogen atoms.

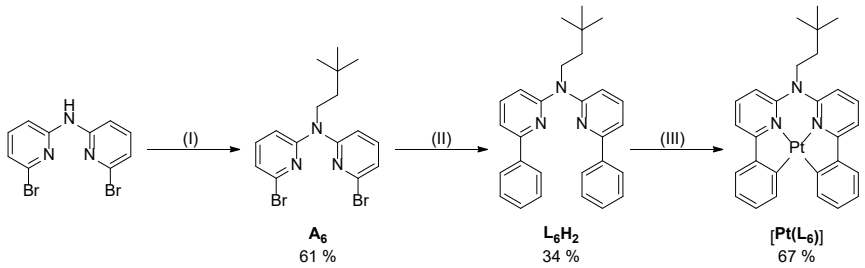

Figure 5. Synthetic route towards complexes with tetradentate ligands. (I) Alkylation: 1-bromo-3,3-dimethyl-butane, NaH, DMF, room temperature, 16 h, 61% yield. (II) Suzuki–Miyaura cross-coupling: phenyl-boronic acid, K_2CO_3, [Pd(PPh$_3$)$_4$], THF, H_2O, reflux, 16 h, 34% yield. (III) Cyclometallation: $K_2[PtCl_4]$, $^nBu_4NCl$, glacial acetic acid, reflux, 16 h, 67% yield.

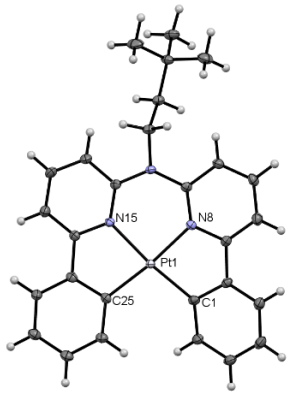

Figure 6. Molecular structure in the single crystal of **[Pt(L$_6$)]**. Displacement ellipsoids are shown at 50% probability.

3.3. Photophysics

The photophysical properties of all the complexes are summarized in Table 1; the absorption and photoluminescence spectra in fluid solutions at 298 K and in frozen glassy matrices at 77 K are shown in Figure 7 (as representative examples including **[PtCl(L$_5$)]** and **[Pt(L$_6$)]**; the complete set of spectra, photoluminescence decay plots, as well as the uncertainties and the multiexponential lifetime components are found in the Supplementary Materials, see Table S5 and Figures S115–S137).

The assignment of the absorption bands by comparison with related compounds [37–39] indicates that the higher-energy bands with strong absorption coefficients below 350 nm correspond to transitions into $^1\pi\pi^*$ configurations (i.e., with ligand-centered character). The lower-energy bands around 375 nm and above can be generally assigned to transitions into mixed charge-transfer states. The UV/Vis spectra (Figure S115) for **[PtCl(L$_{1\text{-}3}$)]** and **[PtCl(L$_5$)]** strongly resemble the reported profile of **[PtCl(L$_0$)]**, suggesting that the alkyl groups have no significant effect on the optical transitions. However, for the amide-substituted complex **[PtCl(L$_4$)]**, a small red shift ($\Delta\lambda \approx 8$ nm) is observable, indicating that the electron-withdrawing effect of the amide substituent affects the energy of the excited electronic states. For complex **[Pt(L$_6$)]**, the bands have distinct features: they are more intense and a low-energy band with an intense absorption at λ_{abs} = 404 nm becomes visible, suggesting a higher charge-transfer character in the excited state. The complexes bearing tridentate

ligands and a chlorido co-ligand exhibit very weak luminescence at room temperature, due to the low LFS caused by the monodentate moiety that acts as an efficient π-donor. This leads to emission spectra with poor signal-to-noise ratios for **[PtCl(L$_4$)]** while impairing the measurement of reliable photoluminescence data at room temperature. As a result of the bis-cyclometalation with an intrinsically higher LFS and rigidity from the tetradentate chromophore, **[Pt(L$_6$)]** shows the best performance.

Table 1. Selected photophysical data for the complexes. A complete set of data is provided in the Supplementary Materials (see Table S5).

Complex	λ_{abs} / nm (ε / 10^3 M^{-1} cm^{-1})	Medium (T / K)	λ_{em} / nm	τ_{av} [a]	$\Phi_L \pm 0.02 / \pm 0.05$ [b]
[PtCl(L$_0$)] [40]	246 (12.5), 266 (20.1), 278 (18.1), 316 (8.1), 348 (8.3), 370 (5.2)	DCM, Ar (298)	496	19.1 ns	<0.02
		Glassy matrix (77)	487	31.8 µs	0.98
[PtCl(L$_1$)]	266 (17.8), 279 (17.4), 314 (6.7), 348 (6.6), 370 (3.7)	DCM, Ar (298)	495	14.58 ns	<0.02
		Glassy matrix (77)	483	23.52 µs	0.98
[PtCl(L$_2$)]	266 (19.9), 280 (17.4), 291 (13.5), 315 (8.2), 349 (8.3), 371 (5.0)	DCM, Ar (298)	495	15.94 ns	<0.02
		Glassy matrix (77)	487	32.86 µs	0.98
[PtCl(L$_3$)]	267 (30.1), 267 (27.7), 316 (10.9), 348 (11.7), 368 (6.7)	DCM, Ar (298)	496	25.7 ns	<0.02
		Glassy matrix (77)	484	24.879 µs	0.98
[PtCl(L$_4$)]	273 (17.7), 293 (15.0), 345 (5.4), 378 (3.3)	DCM, Ar (298)	504	n.d.	n.d.
		Glassy matrix (77)	487	12.42 µs	0.98
[PtCl(L$_5$)]	262 (22.6), 276 (20.9), 288 (16.1), 313 (9.0), 346 (8.6), 370 (5.1)	DCM, Ar (298)	493	0.2695 µs	<0.02
		Glassy matrix (77)	488	45.7 µs	0.98
[Pt(L$_6$)]	274 (43.9), 290 (33.0), 318 (23.5), 334 (22.1), 366 (16.8), 404 (7.2)	DCM, Ar (298)	510	4.2035 µs	0.54
		Glassy matrix (77)	500	11.436 µs	0.97

(a) λ_{exc} = 376 nm, expressed as amplitude-weighted averaged lifetimes according to the suggestions from the relevant literature [49] (the single exponential components, relative amplitudes, and uncertainties are listed in the Supplementary Materials, see Table S5). (b) The uncertainty for the glassy matrix is estimated as $\pm$ 0.05 due to the measurement setup.

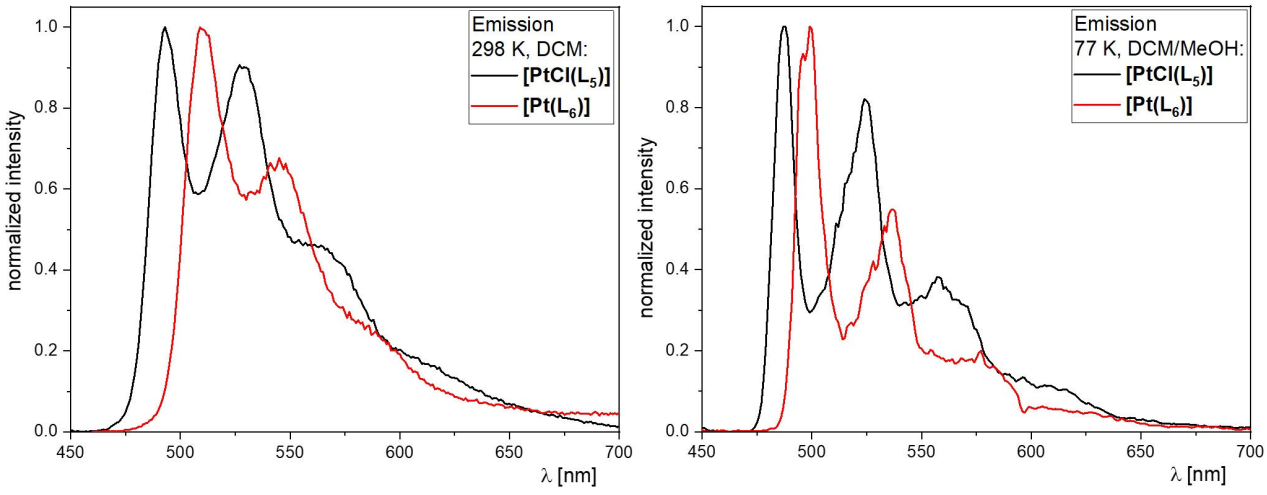

Figure 7. Selected normalized photoluminescence spectra ($\lambda_{exc} \approx$ 370 nm) for **[PtCl(L$_5$)]** (black) and **[Pt(L$_6$)]** (red). Measured in Ar-purged fluid DCM at 298 K (**left**) or in frozen glassy matrices (DCM/MeOH 1:1) at 77 K (**right**).

As the emission maxima peak at around λ_{em} = 495 nm, with a typical vibrational progression, excited state lifetimes (τ_{av}) in the ns range, and photoluminescence quantum yields (Φ_L) below the detection limit of our equipment at room temperature, the complexes **[PtCl(L$_{1\text{-}5}$)]** reproduce the already-reported properties observed for **[PtCl(L$_0$)]**. For **[PtCl(L$_{0\text{-}4}$)]**, the deactivation of the luminescent triplet state is too fast to be affected by oxygen. Only **[PtCl(L$_5$)]** shows a longer lifetime ($\tau_{av(Ar)}$ = 0.2695 µs), but it is also not affected by the presence of oxygen. Upon switching from fluid solution at RT to a glassy matrix at 77 K (DCM:MeOH = 1:1), we observed a blue shift ($\Delta\lambda \approx$ 10 nm) of the emission

maxima, due to the loss of solvent stabilization resulting in an enhanced ligand-centered character for the excited state. The long excited state lifetimes also point to a primarily ligand-centered character for the emissive states (τ_{av} = 23.5 µs–45.7 µs); only the amide-substituted complex [**PtCl(L$_4$)**] shows a faster decay of τ_{av} = 12.42 µs. We assume that the bent coordination plane observed in the molecular structure causes a faster deactivation of the excited state. At 77 K, all complexes show Φ_L close to unity, meaning that the fast relaxation at room temperature can be (mostly) attributed to the radiationless deactivation via thermally accessible metal-centered states; in fact, our previous report showed that this can be overcome by increasing the LFS with a suitable co-ligand, e.g., a cyanido unit acting as a π acceptor. Nonetheless, the nearly invariant photophysical properties suggest that the substitution pattern at the bridging amine group has a negligible effect on the excited state character and the concomitant deactivation rates.

The complex with the tetradentate ligand, [**Pt(L$_6$)**], shows a completely different behavior at room temperature compared to the tridentate chelation pattern. The emission maximum is red-shifted ($\Delta\lambda \approx$ 15 nm) and the vibrational progression is less pronounced. Moreover, the excited state of this complex show a strong sensitivity to the presence of oxygen with a prolonged lifetime (τ_{av} = 0.2354 µs to τ_{av} = 4.2035 µs) and enhanced photoluminescence intensity (Φ_L = 0.02 to Φ_L = 0.53) upon deoxygenation of the solution. This distinct behavior can be attributed to the higher LFS, in combination with a higher degree of metal-to-ligand charge-transfer character in the excited state resulting from the exchange of the thiazol and chlorido σ-donors by a second phenylpyridine arm. Still, in the glassy matrix at 77 K, a blue shift ($\Delta\lambda \approx$ 10 nm) was observed compared to room temperature. Due to the lack of thermally accessibly metal-centered states at 77 K, the Φ_L increases to almost unity with τ_{av} = 11.436 µs. These observations and values are in line with other reports [38,40,50].

4. Conclusions

Five coordination compounds bearing tridentate cyclometallated CˆN*N ligands and one Pt(II) complex with a tetradentate bis-cyclometalated CˆN*NˆC luminophore were synthesized and characterized. In summary, we were able to modify the substitution patterns and solubilities without affecting the excited state properties. The complexes with a tridentate ligand show emission from mostly ligand-centered states, leading to fast radiationless deactivation via thermally accessible metal-centered states due to the low LFS resulting from the chlorido co-ligand; however, upon cooling down to 77 K, unitary quantum yields were achieved. On the other hand, the complex [**Pt(L$_6$)**] with the tetradentate chelator displays higher efficiencies (Φ_L = 0.53) and longer lifetimes in fluid solutions at room temperature, mostly due to a higher rigidity and ligand field splitting resulting from cyclometallation and enhanced metal participation in the excited state, which in turn hampers radiationless deactivation pathways and improves the phosphorescence rate, respectively.

The alkylation step constitutes a bottleneck due to the intrinsic amine–imine tautomerism related to the 2-amino-thiazol moiety. However, the attempted acylation followed by the reduction of the amide to the alkylamine failed due to the relatively high lability of the acylated species. In the future, milder reducing will be explored, such as diborane [51,52], as the product should be stable under acidic workup conditions. If successful, the tautomerism-related limitation could be overcome. The synthetic strategy will facilitate future efforts involving tailored substitution patterns for applications such as bioimaging. In this sense, special attention will be devoted to the complex [**PtCl(L$_5$)**]. Hence, the secondary amine bridge can be modified to avoid harsh reaction conditions linked to cyclometallation.

Supplementary Materials: The following supporting information can be downloaded at: https://www.mdpi.com/article/10.3390/chemistry5020084/s1, Figure S1: ^{1}H-NMR spectrum (400 MHz, DCM-d$_2$) of A$_1$. Figure S2: ^{13}C{^{1}H}-NMR spectrum (101 MHz, DCM-d$_2$) of A$_1$. Figure S3: ^{1}H/^{1}H-COSY-NMR spectrum (400 MHz/400 MHz, DCM-d$_2$) of A$_1$. Figure S4: ^{1}H/^{13}C-gHSQC-NMR spectrum (400

MHz/101 MHz, DCM-d_2) of A_1. Figure S5: $^1H/^{13}C$-gHMBC-NMR spectrum (400 MHz/101 MHz, DCM-d_2) of A_1. Figure S6: ^1H-NMR spectrum (500 MHz, DCM-d_2) of I_1. Figure S7: $^{13}C\{^1H\}$-NMR spectrum (101 MHz, DCM-d_2) of I_1. Figure S8: $^1H/^1H$-COSY-NMR spectrum (400 MHz/400 MHz, DCM-d_2) of I_1. Figure S9: $^1H/^{13}C$-gHSQC-NMR spectrum (400 MHz/101 MHz, DCM-d_2) of I_1. Figure S10: $^1H/^{13}C$-gHMBC-NMR spectrum (400 MHz/101 MHz, DCM-d_2) of I_1. Figure S11: ^1H-NMR spectrum (500 MHz, DCM-d_2) of A_2. Figure S12: $^{13}C\{^1H\}$-NMR spectrum (126 MHz, DCM-d_2) of A_2. Figure S13: $^1H/^1H$-COSY-NMR spectrum (500 MHz/500 MHz, DCM-d_2) of A_2. Figure S14: $^1H/^{13}C$-gHSQC-NMR spectrum (500 MHz/126 MHz, DCM-d_2) of A_2. Figure S15: $^1H/^{13}C$-gHMBC-NMR spectrum (500 MHz/126 MHz, DCM-d_2) of A_2. Figure S16: ^1H-NMR spectrum (400 MHz, DCM-d_2) of I_2. Figure S17: $^{13}C\{^1H\}$-NMR spectrum (101 MHz, DCM-d_2) of I_2. Figure S18: $^1H/^1H$-COSY-NMR spectrum (400 MHz/400 MHz, DCM-d_2) of I_2. Figure S19: $^1H/^{13}C$-gHSQC-NMR spectrum (400 MHz/101 MHz, DCM-d_2) of I_2. Figure S20: $^1H/^{13}C$-gHMBC-NMR spectrum (400 MHz/101 MHz, DCM-d_2) of I_2. Figure S21: ^1H-NMR spectrum (400 MHz, DCM-d_2) of A_3. Figure S22: $^{13}C\{^1H\}$-NMR spectrum (101 MHz, DCM-d_2) of A_3. Figure S23: $^1H/^1H$-COSY-NMR spectrum (400 MHz/400 MHz, DCM-d_2) of A_3. Figure S24: $^1H/^{13}C$-gHSQC-NMR spectrum (400 MHz/101 MHz, DCM-d_2) of A_3. Figure S25: $^1H/^{13}C$-gHMBC-NMR spectrum (400 MHz/101 MHz, DCM-d_2) of A_3. Figure S26: ^1H-NMR spectrum (400 MHz, DCM-d_2) of I_3. Figure S27: $^{13}C\{^1H\}$-NMR spectrum (101 MHz, DCM-d_2) of I_3. Figure S28: $H/^1H$-COSY-NMR spectrum (400 MHz/400 MHz, DCM-d_2) of I_3. Figure S29: $^1H/^{13}C$-gHSQC-NMR spectrum (400 MHz/101 MHz, DCM-d_2) of I_3. Figure S30: $^1H/^{13}C$-gHMBC-NMR spectrum (400 MHz/101 MHz, DCM-d_2) of I_3. Figure S31: ^1H-NMR spectrum (400 MHz, DCM-d_2) of A_4. Figure S32: $^{13}C\{^1H\}$-NMR spectrum (101 MHz, DCM-d_2) of A_4. Figure S33: $^1H/^1H$-COSY-NMR spectrum (400 MHz/400 MHz, DCM-d_2) of A_4. Figure S34: $^1H/^{13}C$-gHSQC-NMR spectrum (400 MHz/101 MHz, DCM-d_2) of A_4. Figure S35: $^1H/^{13}C$-gHMBC-NMR spectrum (400 MHz/101 MHz, DCM-d_2) of A_4. Figure S36: ^1H-NMR spectrum (500 MHz, DCM-d_2) of L_1H. Figure S37: $^{13}C\{^1H\}$-NMR spectrum (126 MHz, DCM-d_2) of L_1H. Figure S38: $^1H/^1H$-COSY-NMR spectrum (500 MHz/500 MHz, DCM-d_2) of L_1H. Figure S39: $^1H/^{13}C$-gHSQC-NMR spectrum (500 MHz/126 MHz, DCM-d_2) of L_1H. Figure S40: $^1H/^{13}C$-gHMBC-NMR spectrum (500 MHz/126 MHz, DCM-d_2) of L_1H. Figure S41: ^1H-NMR spectrum (500 MHz, DCM-d_2) of L_2H. Figure S42: $^{13}C\{^1H\}$-NMR spectrum (101 MHz, DCM-d_2) of L_2H. Figure S43: $^1H/^1H$-COSY-NMR spectrum (400 MHz/400 MHz, DCM-d_2) of L_2H. Figure S44: $^1H/^{13}C$-gHSQC-NMR spectrum (400 MHz/101 MHz, DCM-d_2) of L_2H. Figure S45: $^1H/^{13}C$-gHMBC-NMR spectrum (400 MHz/101 MHz, DCM-d_2) of L_2H. Figure S46: ^1H-NMR spectrum (400 MHz, DCM-d_2) of L_3H. Figure S47: $^{13}C\{^1H\}$-NMR spectrum (101 MHz, DCM-d_2) of L_3H. Figure S48: $^1H/^1H$-COSY-NMR spectrum (400 MHz/400 MHz, DCM-d_2) of L_3H. Figure S49: $^1H/^{13}C$-gHSQC-NMR spectrum (400 MHz/101 MHz, DCM-d_2) of L_3H. Figure S50: $^1H/^{13}C$-gHMBC-NMR spectrum (400 MHz/101 MHz, DCM-d_2) of L_3H. Figure S51: ^1H-NMR spectrum (500 MHz, $CDCl_3$) of L_4H. Figure S52: $^{13}C\{^1H\}$-NMR spectrum (126 MHz, $CDCl_3$) of L_4H. Figure S53: $^1H/^1H$-COSY-NMR spectrum (500 MHz/500 MHz, $CDCl_3$) of L_4H. Figure S54: $^1H/^{13}C$-gHSQC-NMR spectrum (500 MHz/126 MHz, $CDCl_3$) of L_4H. Figure S55: $^1H/^{13}C$-gHMBC-NMR spectrum (500 MHz/126 MHz, $CDCl_3$) of L_4H. Figure S56: ^1H-NMR spectrum (500 MHz, DMSO-d_6) of [PtCl(L_1)]. Figure S57: $^{13}C\{^1H\}$-NMR spectrum (126 MHz, DMSO-d_6) of [PtCl(L_1)]. Figure S58: ^{195}Pt-NMR spectrum (107 MHz, DMSO-d_6) of [PtCl(L_1)]. Figure S59: $^1H/^1H$-COSY-NMR spectrum (500 MHz/500 MHz, DMSO-d_6) of [PtCl(L_1)]. Figure S60: $^1H/^{13}C$-gHSQC-NMR spectrum (500 MHz/126 MHz, DMSO-d_6) of [PtCl(L_1)]. Figure S61: $^1H/^{13}C$-gHMBC-NMR spectrum (500 MHz/126 MHz, DMSO-d_6) of [PtCl(L_1)]. Figure S62: ^1H-NMR spectrum (400 MHz, DCM-d_2/MeOD-d_4) of [PtCl(L_2)]. Figure S63: $^{13}C\{^1H\}$-NMR spectrum (101 MHz, DCM-d_2/MeOD-d_4) of [PtCl(L_2)]. Figure S64: ^{195}Pt-NMR spectrum (107 MHz, DCM-d_2/MeOD-d_4) of [PtCl(L_2)]. Figure S65: $^1H/^1H$-COSY-NMR spectrum (400 MHz/400 MHz, DCM-d_2/MeOD-d_4) of [PtCl(L_2)]. Figure S66: $^1H/^{13}C$-gHSQC-NMR spectrum (400 MHz/101 MHz, DCM-d_2/MeOD-d_4) of [PtCl(L_2)]. Figure S67: $^1H/^{13}C$-gHMBC-NMR spectrum (400 MHz/101 MHz, DCM-d_2/MeOD-d_4) of [PtCl(L_2)]. Figure S68: ^1H-NMR spectrum (500 MHz, DCM-d_2) of [PtCl(L_3)]. Figure S69: $^{13}C\{^1H\}$-NMR spectrum (101 MHz, DCM-d_2) of [PtCl(L_3)]. Figure S70: ^{195}Pt-NMR spectrum (107 MHz, DCM-d_2) of [PtCl(L_3)]. Figure S71: $^1H/^1H$-COSY-NMR spectrum (400 MHz/400 MHz, DCM-d_2) of [PtCl(L_3)]. Figure S72: $^1H/^{13}C$-gHSQC-NMR spectrum (400 MHz/101 MHz, DCM-d_2) of [PtCl(L_3)]. Figure S73: $^1H/^{13}C$-gHMBC-NMR spectrum (400 MHz/101 MHz, DCM-d_2) of [PtCl(L_3)]. Figure S74: ^1H-NMR spectrum (400 MHz, DCM-d_2) of [PtCl(L_4)]. Figure S75: $^{13}C\{^1H\}$-NMR spectrum (101 MHz, DCM-d_2) of [PtCl(L_4)]. Figure S76: ^{195}Pt-NMR spectrum (86 MHz, DCM-d_2) of [PtCl(L_4)]. Figure S77: $^1H/^1H$-COSY-NMR spectrum (400 MHz/400 MHz, DCM-d_2) of [PtCl(L_4)]. Figure S78: $^1H/^{13}C$-gHSQC-NMR spectrum (400 MHz/101 MHz, DCM-d_2) of [PtCl(L_4)]. Figure S79: $^1H/^{13}C$-gHMBC-NMR spectrum (400 MHz/101 MHz, DCM-d_2) of [PtCl(L_4)]. Figure S80: ^1H-NMR spectrum (400 MHz, DMSO-d_6) of [PtCl(L_5)]. Figure S81: $^{13}C\{^1H\}$-NMR spectrum (101 MHz, DMSO-d_6) of [PtCl(L_5)]. Figure S82: ^{195}Pt-NMR spectrum (86 MHz, DMSO-d_6) of [PtCl(L_5)]. Figure S83: $^1H/^1H$-

COSY-NMR spectrum (400 MHz/400 MHz, DMSO-d_6) of [PtCl(L_5)]. Figure S84: ^{1}H/^{13}C-gHSQC-NMR spectrum (400 MHz/101 MHz, DMSO-d_6) of [PtCl(L_5)]. Figure S85: ^{1}H/^{13}C-gHMBC-NMR spectrum (400 MHz/101 MHz, DMSO-d_6) of [PtCl(L_5)]. Figure S86: ^{1}H-NMR spectrum (400 MHz, DCM-d_2) of A_6. Figure S87: ^{13}C{^{1}H}-NMR spectrum (101 MHz, DCM-d_2) of A_6. Figure S88: ^{1}H/^{1}H-COSY-NMR spectrum (400 MHz/400 MHz, DCM-d_2) of A_6. Figure S89: ^{1}H/^{13}C-gHSQC-NMR spectrum (400 MHz/101 MHz, DCM-d_2) of A_6. Figure S90: ^{1}H/^{13}C-gHMBC-NMR spectrum (400 MHz/101 MHz, DCM-d_2) of A_6. Figure S91: ^{1}H-NMR spectrum (500 MHz, $CDCl_3$) of L_6H_2. Figure S92: ^{13}C{^{1}H}-NMR spectrum (126 MHz,$CDCl_3$) of L_6H_2. Figure S93: ^{1}H/^{1}H-COSY-NMR spectrum (500 MHz/500 MHz, $CDCl_3$) of L_6H_2. Figure S94: ^{1}H/^{13}C-gHSQC-NMR spectrum (500 MHz/126 MHz, $CDCl_3$) of L_6H_2. Figure S95: ^{1}H/^{13}C-gHMBC-NMR spectrum (500 MHz/126 MHz, $CDCl_3$) of L_6H_2. Figure S96: ^{1}H-NMR spectrum (400 MHz, DCM-d_2) of L_6BrH. Figure S97: ^{13}C{^{1}H}-NMR spectrum (101 MHz, DCM-d_2) of L_6BrH. Figure S98: ^{1}H/^{1}H-COSY-NMR spectrum (400 MHz/400 MHz, DCM-d_2) of L_6BrH. Figure S99: ^{1}H/^{13}C-gHSQC-NMR spectrum (400 MHz/101 MHz, DCM-d_2) of L_6BrH. Figure S100: ^{1}H/^{13}C-gHMBC-NMR spectrum (400 MHz/101 MHz, DCM-d_2) of L_6BrH. Figure S101: ^{1}H-NMR spectrum (500 MHz, DCM-d_2) of [PtL_6]. Figure S102: ^{13}C{^{1}H}-NMR spectrum (101 MHz, DCM-d_2) of [PtL_6]. Figure S103: ^{195}Pt-NMR spectrum (86 MHz, DCM-d_2) of [PtL_6]. Figure S104: ^{1}H/^{1}H-COSY-NMR spectrum (400 MHz/400 MHz, DCM-d_2) of [PtL_6]. Figure S105: ^{1}H/^{13}C-gHSQC-NMR spectrum (400 MHz/101 MHz, DCM-d_2) of [PtL_6]. Figure S106: ^{1}H/^{13}C-gHMBC-NMR spectrum (400 MHz/101 MHz, DCM-d_2) of [PtL_6]. Figure S107: Molecular structure of compound I_1 in a single crystal and display of the packing. Figure S108: Molecular structure of compound A_3 in a single crystal and display of the packing. Figure S109: Molecular structure of compound A_4 in a single crystal and display of the packing. Figure S110: Molecular structure of compound [PtCl(L_2)] in a single crystal and display of the packing. Figure S111: Molecular structures of compound [PtCl(L_4)] in a single crystal and the display of the distortion of the coordination plane for all three different molecules. Figure S112: Asymetric cell of the crystal structure of [PtCl(L_4)]. Figure S113: Display of the crystal packing of [PtCl(L_4)]. Figure S114: Molecular structure of compound [Pt(L_6)] in a single crystal and display of the packing. Figure S115: Molar absorption coefficient of [PtCl(L_1)], [PtCl(L_2)], [PtCl(L_3)], [PtCl(L_4)], [PtCl(L_5)] and [Pt(L_6)]. Figure S116: Excitation and emission spectra of [PtCl(L_1)] at 298 K in fluid DCM and at 77 K in a frozen glassy DCM/MeOH matrix. Figure S117: Left: Raw (experimental) time-resolved photoluminescence decay of [PtCl(L_1)] in fluid DCM at 298 K (air-equilibrated), including the residuals. Figure S118: Left: Raw (experimental) time-resolved photoluminescence decay of [PtCl(L_1)] in fluid DCM at 298 K (Ar-purged), including the residuals. Figure S119: Left: Raw (experimental) time-resolved photoluminescence decay of [PtCl(L_1)] in a frozen glassy DCM/MeOH matrix at 77 K, including the residuals. Figure S120: Excitation and emission spectra of [PtCl(L_2)] at 298 K in fluid DCM as a solid and at 77 K in a frozen glassy DCM/MeOH matrix. Figure S121: Left: Raw (experimental) time-resolved photoluminescence decay of [PtCl(L_2)] in fluid DCM at 298 K (air-equilibrated), including the residuals. Figure S122: Left: Raw (experimental) time-resolved photoluminescence decay of [PtCl(L_2)] in fluid DCM at 298 K (Ar-purged), including the residuals. Figure S123: Left: Raw (experimental) time-resolved photoluminescence decay of [PtCl(L_2)] in a frozen glassy DCM/MeOH matrix at 77 K, including the residuals. Figure S124: Excitation and emission spectra of [PtCl(L_3)] at 298 K in fluid DCM, at 77 K in a frozen glassy DCM/MeOH matrix and as a solid. Figure S125: Left: Raw (experimental) time-resolved photoluminescence decay of [PtCl(L_3)] in fluid DCM at 298 K (air-equilibrated), including the residuals and IRF. Figure S126: Left: Raw (experimental) time-resolved photoluminescence decay of [PtCl(L_3)] in fluid DCM at 298 K (Ar-purged), including the residuals and IRF. Figure S127: Left: Raw (experimental) time-resolved photoluminescence decay of [PtCl(L_3)] in a frozen glassy DCM/MeOH matrix at 77 K, including the residuals. Figure S128: Excitation and emission spectra of [PtCl(L_4)] at 298 K in fluid DCM and at 77 K in a frozen glassy DCM/MeOH matrix. Figure S129: Left: Raw (experimental) time-resolved photoluminescence decay of [PtCl(L_4)] in a frozen glassy DCM/MeOH matrix at 77 K, including the residuals. Figure S130: Excitation and emission spectra of [PtCl(L_5)] at 298 K in fluid DCM, at 77 K in a frozen glassy DCM/MeOH matrix and as a solid. Figure S131: Left: Raw (experimental) time-resolved photoluminescence decay of [PtCl(L_5)] in fluid DCM at 298 K (air-equilibrated), including the residuals. Figure S132: Left: Raw (experimental) time-resolved photoluminescence decay of [PtCl(L_5)] in fluid DCM at 298 K (Ar-purged), including the residuals. Figure S133: Left: Raw (experimental) time-resolved photoluminescence decay of [PtCl(L_5)] in a frozen glassy DCM/MeOH matrix at 77 K, including the residuals. Figure S134: Excitation and emission spectra of [Pt(L_6)] at 298 K in fluid DCM, at 77 K in a frozen glassy DCM/MeOH matrix and as a solid. Figure S135: Left: Raw (experimental) time-resolved photoluminescence decay of [Pt(L_6)] in fluid DCM at 298 K (air-equilibrated), including the residuals. Figure S136: Left: Raw (experimental) time-resolved photoluminescence decay of [Pt(L_6)] in fluid DCM at 298 K (Ar-purged), including the residuals. Figure S137: Left: Raw (experimental) time-resolved photoluminescence decay of [Pt(L_6)] in a frozen glassy DCM/MeOH

matrix at 77 K, including the residuals. Table S1: Parameters and data from the single crystal measurements. Table S2: Selected bond lengths and angles for [PtCl(L_2)]. Table S3: Selected bond lengths and angles for [PtCl(L_4)]. Table S4: Selected bond lengths and angles for [Pt(L_6)]. Table S5: Complete emission data and Φ_L, as well as exited state lifetime data for each complex in DCM at 298 K and in frozen glassy matrix of DCM/MeOH at 77 K. References [41,47] are cited in the Supplementary Materials.

Author Contributions: Conceptualization, S.B. and C.A.S.; validation, M.V.C., S.B. and C.A.S.; formal analysis, S.B.; NMR-measurements, A.H.; NMR-structure analysis, A.H. and S.B., X-ray diffractometry and structure solution, J.K.; photophysical investigation, M.V.C. and S.B.; resources, C.A.S.; data curation, S.B. and M.V.C.; writing—original draft preparation, S.B.; writing—review and editing, M.V.C. and C.A.S.; visualization, S.B.; supervision, C.A.S.; project administration, C.A.S.; funding acquisition, C.A.S. All authors have read and agreed to the published version of the manuscript.

Funding: C.A.S. gratefully acknowledges funding from the Deutsche Forschungsgemeinschaft (DFG, German Research Foundation)—Project-ID 433682494—SFB 1459, as well as Project STR 1186/6-2 within the Priority Programm 2102 "Light-controlled reactivity of metal complexes". C.A.S. gratefully acknowledges the generous financial support for the acquisition of an "Integrated Confocal Luminescence Spectrometer with Spatiotemporal Resolution and Multiphoton Excitation" (DFG/Land NRW: INST 211/915-1 FUGG; DFG EXC1003: "Berufungsmittel").

Data Availability Statement: CCDC 2252944, 2252945, 2252950, 2252953, 2252954, 2252967 contain the supplementary crystallographic data for this paper. These data can be obtained free of charge via www.ccdc.cam.ac.uk/data_request/cif, or by emailing data_request@ccdc.cam.ac.uk, or by contacting The Cambridge Crystallographic Data Center, 12 Union Road, Cambridge CB2 1EZ, UK; fax: +44 1223 226033.

Acknowledgments: S.B. thanks Christiane Terlinde for the help in the synthesis of the **[Pt(L_6)]** complex.

Conflicts of Interest: The authors declare no conflict of interest.

References

1. Wunschel, K.R.; Ohnesorge, W.E. Luminescence of Iridium(II) Chelates with 2,2′-bipyridine and with 1,10-phenanthroline. *J. Am. Chem. Soc.* **1967**, *89*, 2777–2778. [CrossRef]
2. Baldo, M.A.; Lamansky, S.; Thompson, M.E.; Forrest, S.R. Very High-Efficiency Green Organic Light-Emitting Devices Based on Electrophosphorescence. *Appl. Phys. Lett.* **1999**, *75*, 4–6. [CrossRef]
3. Cheung, T.-C.; Cheung, K.-K.; Peng, S.-M.; Che, C.-M. Photoluminescent Cyclometallated Diplatinum(II,II) Complexes: Photophysical Properties and Crystal Structures of [PtL(PPh3)]ClO4 and [Pt2L2(μ-dppm)][ClO4]2(HL = 6-phenyl-2,2′-bipyridine, dppm = Ph2PCH2PPh2). *J. Chem. Soc., Dalton Trans.* **1996**, 1645–1651. [CrossRef]
4. Wong, Y.S.; Tang, M.C.; Ng, M.; Yam, V.W.W. Toward the Design of Phosphorescent Emitters of Cyclometalated Earth Abundant Nickel(II) and Their Supramolecular Study. *J. Am. Chem. Soc.* **2020**, *142*, 7638–7646. [CrossRef] [PubMed]
5. Williams, J.A.G.; Beeby, A.; Davies, E.S.; Weinstein, J.A.; Wilson, C. An Alternantive Rout to Highly Luminescent Platinum(II) Complexes: Cyclometalation with NˆCˆN-Coordinating Dipyridylbenzene Ligands. *Inorg. Chem.* **2003**, *42*, 8609–8611. [CrossRef]
6. Otto, S.; Grabolle, M.; Förster, C.; Kreitner, C.; Resch-Genger, U.; Heinze, U. [Cr(ddpd)2]3+: A Molecular, Water-Soluble, Highly NIR-Emissive Ruby Analogue. *Angew. Chem. Int. Ed.* **2015**, *54*, 11572–11576. [CrossRef]
7. Chow, P.-K.; Cheng, G.; Tong, G.S.M.; To, W.-P.; Kwong, W.-L.; Low, K.-H.; Kwok, C.-C.; Ma, C.; Che, C.-M. Luminescent Pincer Platinum(II) Complexes with Emission Quantum Yields up to Almost Unity: Photophysics, Photoreductive C-C Bond Formation, and Materials Applications. *Angew. Chem. Int. Ed.* **2015**, *54*, 2084–2089. [CrossRef]
8. Sanning, J.; Ewen, P.; Stegemann, L.; Schmidt, J.; Daniliuc, C.G.; Koch, T.; Doltsinis, N.L.; Wegner, D.; Strassert, C.A. Scanning-Tunneling-Spectroscopy-Directed Design of Tailored Deep-Blue Emitters. *Angew. Chem. Int. Ed.* **2015**, *54*, 786–791. [CrossRef]
9. Rossi, E.; Colombo, A.; Dragonetti, C.; Roberto, D.; Ugo, R.; Valore, A.; Falciola, L.; Brulatti, P.; Cocchi, M.; Williams, J.A.G. Novel NˆCˆN-Cyclometallated Platinum Complexes with Acetylide Co-Ligands as Efficient Phosphors for OLEDs. *J. Mater. Chem.* **2012**, *22*, 10650–10655. [CrossRef]
10. Kayano, T.; Takayasu, S.; Sato, K.; Shinozaki, K. Luminescence Color Tuning of PtII Complexes and a Kinetic Study of Trimer Formation in the Photoexcited State. *Chem. Eur. J.* **2014**, *20*, 16583–16589. [CrossRef]
11. Cebrián, C.; Mauro, M. Recent Advances in Phosphorescent Platinum Complexes for Organic Light-Emitting Diodes, Beilstein. *J. Org. Chem.* **2018**, *14*, 1459–1481.
12. Cheng, G.; Kwak, Y.; To, W.P.; Lam, T.L.; Tong, G.S.M.; Sit, M.K.; Gong, S.; Choi, B.; Choi, W.I.; Yang, C.; et al. High-Efficiency Solution-Processed Organic Light-Emitting Diodes with Tetradentate Platinum(II) Emitters. *ACS Appl. Mater. Interfaces* **2019**, *11*, 45161–45170. [CrossRef] [PubMed]
13. Zhang, Y.; Wang, Y.; Song, J.; Qu, J.; Li, B.; Zhu, W.; Wong, W.-Y. Near-Infrared Emitting Materials via Harvesting Triplet Excitons: Molecular Design, Properties, and Application in Organic Light Emitting Diodes. *Adv. Opt. Mater.* **2018**, *6*, 1800466. [CrossRef]

14. Sanning, J.; Stegemann, L.; Ewen, P.R.; Schwermann, C.; Daniliuc, C.G.; Zhang, D.; Lin, N.; Duan, L.; Wegner, D.; Doltsinis, N.L.; et al. Colour-Tunable Asymmetric Cyclometalated Pt(II) Complexes and STM-Assisted Stability Assessment of Ancillary Ligands for OLEDs. *J. Mater. Chem. C* **2016**, *4*, 2560–2565. [CrossRef]
15. Koshevoy, I.O.; Krause, M.; Klein, A. Non-Covalent Intramolecular Interactions through Ligand-Design Promoting Efficient Luminescence from Transition Metal Complexes. *Coord. Chem. Rev.* **2020**, *405*, 213094. [CrossRef]
16. Ravotto, L.; Ceroni, P. Aggregation induced phosphorescence of metal complexes: From principles to applications. *Coord. Chem. Rev.* **2017**, *346*, 62–76. [CrossRef]
17. Nisic, F.; Colombo, A.; Dragonetti, C.; Roberto, D.; Valore, A.; Malicka, J.M.; Cocchi, M.; Freeman, G.R.; Williams, J.A.G. Platinum(II) Complexes with Cyclometallated 5-π-Delocalized-Donor-1,3-di(2-pyridyl)benzene Ligands as Efficient Phosphors for NIROLEDs. *J. Mater. Chem. C* **2014**, *2*, 1791–1800. [CrossRef]
18. Tam, A.Y.-Y.; Tsang, D.P.-K.; Chan, M.-Y.; Zhu, N.; Yam, V.W.-W. A Luminescent Cyclometalated Platinum(II) Complex and its Green Organic Light Emitting Device with High Device Performance. *Chem. Commun.* **2011**, *47*, 3383–3385. [CrossRef]
19. Lu, W.; Mi, B.-X.; Chan, M.C.W.; Hui, Z.; Zhu, N.; Lee, S.-T.; Che, C.-M. [(CˆNˆN)Pt(C≡C)nR] (HCˆNˆN = 6-aryl-2,2′-bipyridine, n = 1-4, R = aryl, SiMe3) as a New Class of Light Emitting Materials and their Applications in Electrophosphorescent Devices. *Chem. Commun.* **2002**, 206–207. [CrossRef]
20. Mao, M.; Peng, J.; Lam, T.-L.; Ang, W.-H.; Li, H.; Cheng, G.; Che, C.-M. High-performance organic light-emitting diodes with low-efficiency roll-off using bulky tetradentate [Pt(OˆNˆCˆN)] emitters. *J. Mater. Chem. C* **2019**, *7*, 7230–7236. [CrossRef]
21. Kalinowski, J.; Fattori, V.; Cocchi, M.; Williams, J.A.G. Light-emitting devices based on organometallic platinum complexes as emitters. *Coord. Chem. Rev.* **2011**, *255*, 2401–2425. [CrossRef]
22. Yersin, H.; Rausch, A.F.; Czerwieniec, R.; Hofbeck, T.; Fischer, T. The triplet state of organo-transition metal compounds. Triplet harvesting and singlet harvesting for efficient OLEDs. *Coord. Chem. Rev.* **2011**, *255*, 2622–2652. [CrossRef]
23. Zhong, J.-J.; Meng, Q.-Y.; Wang, G.-X.; Liu, Q.; Chen, B.; Feng, K.; Tung, C.-H.; Wu, L.-Z. A Highly Efficient and Selective Aerobic Cross-Dehydrogenative-Coupling Reaction Photocatalyzed by a Platinum(II) Terpyridyl Complex. Chem. *Eur. J.* **2013**, *19*, 6443–6450. [CrossRef] [PubMed]
24. Mori, K.; Yamashita, H. Metal Complexes Supported on Solid Matrices for Visible-Light-Driven Molecular Transformations. *Chem. Eur. J.* **2016**, *22*, 11122–11137. [CrossRef] [PubMed]
25. Parasram, M.; Gevorgyan, V. Visible light-induced transition metal-catalyzed transformations: Beyond conventional photosensitizers. *Chem. Soc. Rev.* **2017**, *46*, 6227–6240. [CrossRef] [PubMed]
26. Choi, W.J.; Choi, S.; Ohkubo, K.; Fukuzumi, S.; Cho, E.J.; You, Y. Mechanisms and applications of cyclometalated Pt(II) complexes in photoredox catalytic trifluoromethylation. *Chem. Sci.* **2015**, *6*, 1454–1464. [CrossRef]
27. Wu, P.; Wong, E.L.-M.; Ma, D.-L.; Tong, G.S.-M.; Ng, K.-M.; Che, C.-M. Cyclometalated Platinum(II) Complexes as Highly Sensitive Luminescent Switch-On Probes for Practical Application in Protein Staining and Cell Imaging. *Chem. Eur. J.* **2009**, *15*, 3652–3656. [CrossRef]
28. Chung, C.Y.-S.; Li, S.P.-Y.; Louie, M.-W.; Lo, K.K.-W.; Yam, V.W.-W. Induced Self-Assembly and Disassembly of Water-Soluble Alkynylplatinum(II) Terpyridyl Complexes with "Switchable" NearInfrared (NIR) Emission Modulated by Metal-Metal Interaction over Physiological pH: Demonstration of pH-Responsive NIR Luminescent Probes in Cell-Imaging Studies. *Chem. Sci.* **2013**, *4*, 2453–2462. [CrossRef]
29. Baggaley, E.; Botchway, S.W.; Haycock, J.W.; Morris, H.; Sazanovich, I.V.; Williams, J.A.G.; Weinstein, J.A. Long-Lived Metal Complexes open up Microsecond Lifetime Imaging Microscopy under Multiphoton Excitation: From FLIM to PLIM and beyond. *Chem. Sci.* **2014**, *5*, 879–886. [CrossRef]
30. Zhang, K.Y.; Yu, Q.; Wei, H.; Liu, S.; Zhao, Q.; Huang, W. Long-Lived Emissive Probes for Time-Resolved Photoluminescence Bioimaging and Biosensing. *Chem. Rev.* **2018**, *118*, 1770–1839. [CrossRef]
31. Guerchais, V.; Fillaut, J.-L. Sensory Luminescent Iridium(III) and Platinum(II) Complexes for Cation Recognition. *Coord. Chem. Rev.* **2011**, *255*, 2448–2457. [CrossRef]
32. Ma, D.-L.; Ma, V.P.-Y.; Chan, D.S.-H.; Leung, K.-H.; He, H.-Z.; Leung, C.-H. Recent Advances in Luminescent Heavy Metal Complexes for Sensing. *Coord. Chem. Rev.* **2012**, *256*, 3087–3113. [CrossRef]
33. Liu, L.; Wang, X.; Hussain, F.; Zeng, C.; Wang, B.; Li, Z.; Kozin, I.; Wang, S. Multiresponsive Tetradentate Phosphorescent Metal Complexes as Highly Sensitive and Robust Luminescent Oxygen Sensors: Pd(II) Versus Pt(II) and 1,2,3-Triazolyl Versus 1,2,4-Triazolyl. *ACS Appl. Mater. Interfaces* **2019**, *11*, 12666–12674. [CrossRef] [PubMed]
34. Li, K.; Tong, G.S.M.; Wan, Q.; Cheng, G.; Tong, W.-Y.; Ang, W.-H.; Kwong, W.-L.; Che, C.-M. Highly Phosphorescent Platinum(II) Emitters: Photophysics, Materials and Biological Application. *Chem. Sci.* **2016**, *7*, 1653–1673. [CrossRef]
35. Williams, J.A.G. Photochemistry and Photophysics of Coordination Compounds II. Top. *Curr. Chem.* **2007**, *281*, 205–268.
36. Wu, W.; Huang, D.; Zhao, J. Tridentate Cyclometalated Platinum(II) Complexes with Strong Absorption of Visible Light and Long-Lived Triplet Excited States as Photosensitizers for Triplet–Triplet Annihilation Upconversion. *Dyes Pigm.* **2013**, *96*, 220–231. [CrossRef]
37. Ravindranathan, D.; Vezzu, D.A.K.; Bartolotti, L.; Boyle, P.D.; Hou, S. Improvement in Phosphorescence Efficiency through Tuning of Coordination Geometry of Tridentate Cyclometalated Platinum(II) Complexes. *Inorg. Chem.* **2010**, *49*, 8922–8928. [CrossRef]

38. Vezzu, D.A.K.; Deaton, J.C.; Jones, J.S.; Bartolotti, L.; Harris, C.F.; Marchetti, A.P.; Kondakova, M.; Pike, R.D.; Huo, S. Highly Luminescent Tetradentate Bis-Cyclometalated Platinum Complexes: Design, Synthesis, Structure, Photophysics, and Electroluminescence Application. *Inorg. Chem.* **2010**, *49*, 5107–5119. [CrossRef]
39. Wilde, S.; Ma, D.; Koch, T.; Bakker, A.; Gonzalez-Abradelo, D.; Stegemann, L.; Daniliuc, C.G.; Fuchs, H.; Gao, H.; Doltsinis, N.L.; et al. Toward Tunable Electroluminescent Devices by Correlating Function and Submolecular Structure in 3D Crystals, 2D-Confined Monolayers, and Dimers. *ACS Appl. Mater. Interfaces* **2018**, *10*, 22460–22473. [CrossRef]
40. Ren, J.; Cnudde, M.; Brünink, D.; Buss, S.; Daniliuc, C.G.; Liu, L.; Fuchs, H.; Strassert, C.A.; Gao, H.-Y.; Doltsinis, N.L. On-Surface Reactive Planarization of Pt(II) Complexes. *Angew. Chem. Int. Ed.* **2019**, *58*, 15396–15400. [CrossRef]
41. Knedel, T.-O.; Buss, S.; Maisuls, I.; Daniliuc, C.G.; Schlüsener, C.; Brandt, P.; Weingart, O.; Vollrath, A.; Janiak, C.; Strassert, C.A. Encapsulation of Phosphorescent Pt(II) Complexes in Zn-Based Metal–Organic Frameworks toward Oxygen-Sensing Porous Materials. *Inorg. Chem.* **2020**, *59*, 7252–7264. [CrossRef] [PubMed]
42. Macrae, C.F.; Sovago, I.; Cottrell, S.J.; Galek, P.T.A.; McCabe, P.; Pidcock, E.; Platings, M.; Shields, G.P.; Stevens, J.S.; Towler, M.; et al. Mercury 4.0: From Visualization to Analysis, Design and Prediction. *J. Appl. Cryst.* **2020**, *53*, 226–235. [CrossRef] [PubMed]
43. Schnürch, M.; Waldner, B.; Hilber, K.; Mihovilovic, M.D. Synthesis of 5-arylated N-arylthiazole-2-amines as Potential Skeletal Muscle Cell Differentiation Promoters. *Bioorg. Med. Chem. Lett.* **2011**, *21*, 2149–2154. [CrossRef] [PubMed]
44. Dao-Huy, T.; Waldner, B.; Wimmer, L.; Schnürch, M.; Mihovilovic, M.D. Synthesis of endo- and exo-N-Protected 5-Arylated 2-Aminothiazols through Direct Arylation: An Efficient Route to Cell Differentiation Accelerators. *Eur. J. Org. Chem.* **2015**, 4765–4771. [CrossRef]
45. Sintenis, F. Beiträge zur Kenntniss der Benzyläther. *Liebigs Ann. Chem.* **1872**, *161*, 329–346. [CrossRef]
46. Lai, S.-W.; Cheung, T.-C.; Chan, M.C.W.; Cheung, K.-K.; Peng, S.-M.; Che, C.-M. Luminescent Mononuclear and Binuclear Cyclometalated Palladium(II) Complexes of 6-Phenyl-2,2′-Bipyridines: Spectroscopic and Structural Comparisons with Platinum(II) Analogues 1,2. *Inorg. Chem.* **2000**, *39*, 255–262. [CrossRef]
47. Zhang, E.-X.; Wang, D.-X.; Huang, Z.-T.; Wang, M.-X. Synthesis of (NH)m(NMe)4−m-Bridged Calix [4]pyridines and the Effect of NH Bridge on Structure and Properties. *J. Org. Chem.* **2009**, *74*, 8595–8603. [CrossRef]
48. Solomatina, A.I.; Galenko, E.E.; Kozina, D.O.; Kalinichev, A.A.; Baigildin, V.A.; Prudovskaya, N.A.; Shakirova, J.R.; Khlebnikov, A.F.; Prosev, V.V.; Evarestov, R.A.; et al. Nonsymmetric [Pt(C^N*N′^C′)] Complexes: Aggregation-Induced Emission in the Solid State and in Nanoparticles Tuned by Ligand Structure. *Chem. Eur. J.* **2022**, *28*, e202202207. [CrossRef]
49. Sillen, A.; Engelborghs, Y. The Correct Use of "Average" Fluorescence Parameters. *Photochem. Photobiol.* **1998**, *67*, 475–486. [CrossRef]
50. Wilde, S.; Mittelberg, L.; Daniliuc, C.G.; Koch, T.; Doltsinis, N.L.; Strassert, C.A. Studie über den Einfluss des Fluorierungsgrades an einem tetradentaten C^N*N^C-Luminophor auf die photophysikalischen Eigenschaften seiner Platin(II)-Komplexe und deren Aggregation. *Z. Naturforsch.* **2018**, *73*, 849–863. [CrossRef]
51. Strassert, C.A.; Dicelio, L.E.; Awruch, J. Reduction of an Amido Zinc(II) Phthalocyanine by Diborane. *Synthesis* **2006**, *5*, 799–802. [CrossRef]
52. Strassert, C.A.; Awruch, J. Conversion of Phthalimides to Isoinddolines by Diborane. *Monatsh. Chem.* **2006**, *137*, 1499–1503. [CrossRef]

Disclaimer/Publisher's Note: The statements, opinions and data contained in all publications are solely those of the individual author(s) and contributor(s) and not of MDPI and/or the editor(s). MDPI and/or the editor(s) disclaim responsibility for any injury to people or property resulting from any ideas, methods, instructions or products referred to in the content.